mater.scichina.com link.springer.com

Published online 12 August 2021 | https://doi.org/10.1007/s40843-021-1739-0
Sci China Mater 2022, 65(2): 356–363

In situ construction of heterostructured bimetallic sulfide/phosphide with rich interfaces for high-performance aqueous Zn-ion batteries

Fang Yang[1], Yuenian Shen[2], Ze Cen[1], Jie Wan[1], Shijie Li[3*], Guanjie He[4], Junqing Hu[2,5] and Kaibing Xu[2*]

ABSTRACT **It is still challenging to develop suitable cathode structures for high-rate and stable aqueous Zn-ion batteries. Herein, a phosphating-assisted interfacial engineering strategy is designed for the controllable conversion of $NiCo_2S_4$ nanosheets into heterostructured $NiCoP/NiCo_2S_4$ as the cathodes in aqueous Zn-ion batteries. The multicomponent heterostructures with rich interfaces can not only improve the electrical conductivity but also enhance the diffusion pathways for Zn-ion storage. As expected, the $NiCoP/NiCo_2S_4$ electrode has high performance with a large specific capacity of 251.1 mA h g^{-1} at a high current density of 10 A g^{-1} and excellent rate capability (retaining about 76% even at 50 A g^{-1}). Accordingly, the Zn-ion battery using $NiCoP/NiCo_2S_4$ as the cathode delivers a high specific capacity (265.1 mA h g^{-1} at 5 A g^{-1}), a long-term cycling stability (96.9% retention after 5000 cycles), and a competitive energy density (444.7 W h kg^{-1} at the power density of 8.4 kW kg^{-1}). This work therefore provides a simple phosphating-assisted interfacial engineering strategy to construct heterostructured electrode materials with rich interfaces for the development of high-performance energy storage devices in the future.**

Keywords: phosphating, heterostructure, $NiCoP/NiCo_2S_4$, Zn-ion batteries, high capacity

INTRODUCTION

To alleviate the excessive consumption of traditional fossil fuels and increasing environmental pollution issues, it is particularly urgent and important to develop high-efficiency and clean energy storage devices. Typically, lithium (Li)-ion batteries have been widely used in a variety of energy storage systems, such as portable electronics, electric vehicles, and grid-scale energy-storage systems [1]. However, the large-scale application of Li-ion batteries is still a huge challenge because of limited lithium resources and toxic organic electrolytes [2–5]. Recently, researchers have focused on the exploration of high-performance aqueous rechargeable batteries with low cost and reliable safety [6–10]. Among various rechargeable batteries, aqueous Zn-ion batteries are emerging as one of the most competitive candidates to replace Li-ion batteries by virtue of the high theoretical capacity of the zinc anode (820 mA h g^{-1}), high working voltage (~1.8 V), as well as its low cost and low toxicity [11–20]. However, the unsatisfactory energy/power density and poor cycling stability severely limit their practical application. Designing and constructing highly active cathode materials has been demonstrated as a promising strategy to improve the performance of Zn-ion batteries.

Transition metal sulfides have been extensively investigated as electrode materials due to their higher electronic conductivity and better reversible electrochemical properties than those of their oxide counterparts [21–24]. Especially, $NiCo_2S_4$ electrode materials have been proved to have better electronic conductivities of about 100 times higher than that of $NiCo_2O_4$ [21,25]. In addition, compared with its corresponding single-component sulphides (NiS_x and CoS_x), $NiCo_2S_4$ has significantly richer redox reactions because of multiple available oxidation states and faster electron transfer properties [26,27]. For instance, Han *et al.* [28] developed sulfur-deficient $NiCo_2S_{4-x}$ nanotube arrays on carbon cloth as an effective cathode material for flexible Zn batteries, which delivered a high capacity of 298.3 mA h g^{-1} at 0.5 A g^{-1} and superior rate capability. On the other hand, transition metal phosphides have attracted extensive research interest due to their unique electronic structure and high thermal/chemical stability, which show high electrocatalytic activity/durability and good conductivity [29–33]. For example, Zhang *et al.* [34] developed ultrafine and highly active bimetallic $Co_xNi_{1-x}P$ nanoparticles loaded on carbon nanofibers, exhibiting an extraordinary specific capacitance of 3514 F g^{-1} at 5 A g^{-1}. Therefore, the *in-situ* construction of metal phosphides based on metal sulfides can effectively realize the coupling of their respective advantages. Furthermore, constructing novel multi-component heterostructures with metal sulfides and phosphides is emerging as an effective strategy to generate abundant interfaces for fast charge transfer and to improve the number of highly exposed active sites for redox reactions, showing great application potential.

In this study, we developed a controllable route to fabricate heterostructured $NiCoP/NiCo_2S_4$ nanosheet arrays on carbon cloth as electrode, which showed the strong synergistic effect and rich interfaces between NiCoP and $NiCo_2S_4$, and delivered a high specific capacity of 251.1 mA h g^{-1} at a high current density

[1] School of Mechanical and Automotive Engineering, Shanghai University of Engineering Science, Shanghai 201620, China
[2] State Key Laboratory for Modification of Chemical Fibers and Polymer Materials, Research Center for Analysis and Measurement & College of Materials Science and Engineering, Donghua University, Shanghai 201620, China
[3] Institute of Innovation & Application, National Engineering Research Center for Marine Aquaculture, Zhejiang Ocean University, Zhoushan 316022, China
[4] School of Chemistry, University of Lincoln, Brayford Pool, Lincoln LN6 7TS, UK
[5] College of Health Science and Environmental Engineering, Shenzhen Technology University, Shenzhen 518118, China
* Corresponding authors (emails: lishijie@zjou.edu.cn (Li S); xukaibing@dhu.edu.cn (Xu K))

of 10 A g^{-1} and excellent rate capability. The aqueous Zn-ion battery based on NiCoP/$NiCo_2S_4$ (NiCoP/$NiCo_2S_4$//Zn battery) delivered a high specific capacity of 265.1 mA h g^{-1} at 5 A g^{-1} and good cycling stability (capacity retention of 96.9% after 5000 cycles). Moreover, this battery possessed a high energy density of 444.7 W h kg^{-1} at the power density of 8.4 kW kg^{-1}. This study verifies that establishing transition metal sulfides and phosphides heterostructured materials for enhancing the energy storage performance of aqueous Zn-ion batteries is efficient.

EXPERIMENTAL SECTION

Synthesis of $NiCo_2S_4$ nanosheet arrays

$Ni(NO_3)_2{\cdot}6H_2O$ (1 mmol), $Co(NO_3)_2{\cdot}6H_2O$ (2 mmol), and hexamethylenetetramine (5.7 mmol) were dissolved in deionized water (25 mL) and ethanol (25 mL) under vigorous stirring. The resulting pink solution was then transferred into a 60-mL stainless steel autoclave with a piece of pretreated carbon cloth (1 cm × 4 cm) and sealed at 95°C for 8 h. Subsequently, the obtained precursor on carbon cloth was annealed in air at 350°C for 2 h, to obtain $NiCo_2O_4$. Finally, the above carbon cloth was immersed in 50 mL of deionized water with 1 g of $Na_2S{\cdot}9H_2O$, and maintained at 100°C for 24 h to obtain $NiCo_2S_4$ samples.

Synthesis of NiCoP/$NiCo_2S_4$ nanosheet arrays

To fabricate the NiCoP/$NiCo_2S_4$ nanosheet arrays, the $NiCo_2S_4$ nanosheet arrays on carbon cloth were annealed under N_2 atmosphere with the presence of NaH_2PO_2 (0.25–1 g) at 350–450°C for 1–4 h. The mass loadings of $NiCo_2S_4$ and NiCoP/$NiCo_2S_4$ materials were 0.60 and 0.63 mg cm^{-2}, respectively. For comparison, the $NiCo_2O_4$ nanosheet arrays were prepared at 400°C for 2 h with 0.5 g of NaH_2PO_2 to obtain NiCoP nanosheet arrays.

Materials characterization

The as-obtained materials were investigated by scanning electron microscopy (SEM; Hitachi, S-4800), transmission electron microscopy (TEM; JEOL, JEM-2100F), X-ray diffractometer (XRD; Rigaku, D/max-2550 PC), X-ray photoelectron spectroscopy (XPS; Thermo Fisher, Escalab 250Xi), and Brunauer-Emmett-Teller analyzer (BET; Quantachrome, Autosorb-iQ).

Electrochemical measurement

The electrochemical measurements were carried out on an electrochemical workstation (Metrohm Autolab PGSTAT302N, the Netherlands). A three-electrode system was assembled for the evaluation of electrochemical properties of individual electrodes in 1 mol L^{-1} KOH aqueous solution. The NiCoP/$NiCo_2S_4$ nanosheet arrays on carbon cloth were used directly as the working electrode, with the saturated calomel electrode as a reference and a platinum plate as the counter electrode. The aqueous Zn-ion battery was assembled using NiCoP/$NiCo_2S_4$ materials as the cathode and a piece of commercial Zn plate as the anode with the mixed solution of 1 mol L^{-1} KOH and 0.01 mol L^{-1} $Zn(CH_3COO)_2$ as the electrolyte, and the two-electrode configuration was constructed to assess the electrochemical performance of the as-fabricated batteries.

RESULTS AND DISCUSSION

Fig. 1 schematically illustrates the entire preparation procedure of heterostructured NiCoP/$NiCo_2S_4$ nanosheet arrays on carbon cloth. First, $NiCo_2O_4$ nanosheets are directly grown on the bare carbon cloth through a facile hydrothermal reaction, and calcined under air atmosphere to improve their crystallinity. After that, hydrothermal reaction is again employed to realize the phase transformation between $NiCo_2O_4$ and $NiCo_2S_4$ by using $Na_2S{\cdot}9H_2O$ as the sulfur source, where all the O^{2-} is exchanged into S^{2-} *via* the Kirkendall effect. Finally, to accomplish the interfacial engineering of $NiCo_2S_4$, phosphate treatment is conducted with NaH_2PO_2 as the phosphorus source. During this process, newly formed NiCoP nanoparticles are embedded into $NiCo_2S_4$ nanosheets, generating an updated heterostructured nanostructure with rich interfaces due to the higher electronegativity of P than those of Ni and Co [35]. The NiCoP/$NiCo_2S_4$ electrode prepared at 400°C for 2 h with 0.5 g of NaH_2PO_2 is discussed in the following sections, unless otherwise stated, as it shows the highest specific capacities.

The micromorphology of the $NiCo_2S_4$ nanosheets on carbon cloth was preliminarily investigated by SEM and TEM (Fig. 2). The SEM images (Fig. 2a, b) show that the $NiCo_2S_4$ nanosheets derived from $NiCo_2O_4$ nanosheets (Fig. S1) remain uniformly supported on the carbon cloth, and these nanosheets are interconnected to each other. In Fig. 2c, the TEM image of the $NiCo_2S_4$ nanosheet shows numerous small pores uniformly distributed throughout the surface. The high-resolution TEM image (HRTEM) characterization clearly displays the lattice fringe with an interplanar distance of 0.332 nm, well corresponding to the (220) plane of $NiCo_2S_4$ (Fig. 2d). Furthermore, the energy dispersive X-ray spectroscopy (EDS) element mapping images (Fig. 2e) show the even distribution of Ni, Co and S

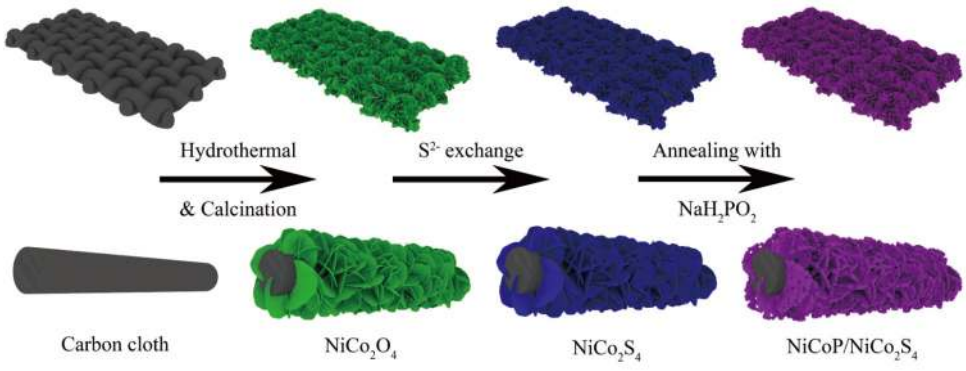

Figure 1 Schematic illustration of the heterostructured NiCoP/$NiCo_2S_4$ nanosheet arrays supported on carbon cloth.

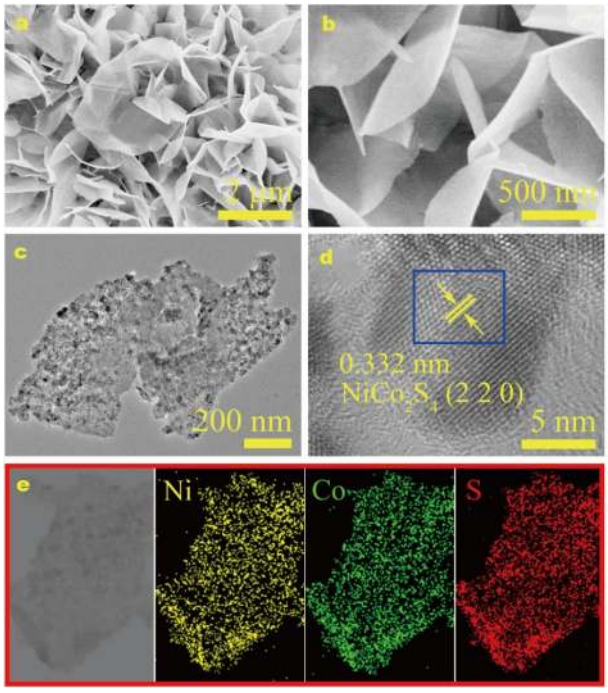

Figure 2 (a, b) SEM, (c) TEM, (d) HRTEM, and (e) elemental mapping images of the $NiCo_2S_4$ nanosheets.

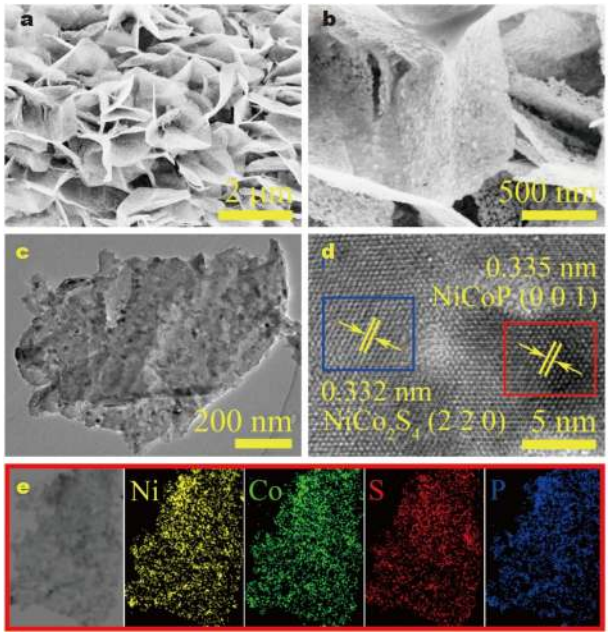

Figure 3 (a, b) SEM, (c) TEM, (d) HRTEM, and (e) the corresponding elemental mapping images of the $NiCoP/NiCo_2S_4$ nanosheets.

elements in the $NiCo_2S_4$ nanosheet.

According to the SEM images of Fig. 3a, b, the densely packed and highly ordered $NiCoP/NiCo_2S_4$ nanosheet arrays are uniformly grown on the carbon cloth surface, and these nanosheets are interconnected to each other with plenty of spaces, which are beneficial to the charge transportation and ion diffusion, thus enhancing the specific capacity. Compared with $NiCo_2S_4$ nanosheets, the surface of the $NiCoP/NiCo_2S_4$ nanosheets becomes much rougher after phosphating treatment due to the formation of NiCoP nanoparticles. Moreover, the effects of phosphating conditions on the morphology of the $NiCoP/NiCo_2S_4$ materials were also systematically investigated by adjusting the treatment temperature, the reaction time and the mass of NaH_2PO_2. As shown in Fig. S2, with the increase of temperature, time and amount of the P source, more NiCoP nanoparticles are generated on the $NiCo_2S_4$ nanosheets. Additionally, the BET surface areas were also tested (Fig. S3). The specific area of $NiCoP/NiCo_2S_4$ is 26.2 $m^2 g^{-1}$, while that of $NiCo_2S_4$ is 27.3 $m^2 g^{-1}$. The decrease in specific surface area may be caused by the newly formed NiCoP nanoparticles plugging the pores in the $NiCo_2S_4$ nanosheets. The formation of heterostructured $NiCoP/NiCo_2S_4$ nanosheets was further confirmed by TEM. As shown in Fig. 3c, NiCoP nanoparticles are distributed on the surface of the $NiCo_2S_4$ nanosheets, which is consistent with the result from SEM analysis. Fig. 3d shows the HRTEM of the $NiCoP/NiCo_2S_4$ nanosheet, and the obvious lattice fringes spaced at 0.332 and 0.335 nm, correspond well to the (220) plane of $NiCo_2S_4$ and (001) plane of NiCoP. The EDS mapping images (Fig. 3e) further confirm that the Ni, Co, S and P elements are uniformly distributed throughout the $NiCoP/NiCo_2S_4$ nanosheet.

The phase of the as-prepared materials was firstly acquired through the analysis of XRD data. As shown in Fig. 4a, the XRD pattern of $NiCoP/NiCo_2S_4$ displays well-defined diffraction peaks, which well match with the standard XRD patterns of $NiCo_2S_4$ (JCPDS No. 73-1704) and NiCoP (JCPDS No. 71-2336), confirming the coexistence of NiCoP and $NiCo_2S_4$ after phosphating treatment without any residues or contaminants. Moreover, XPS was further performed to investigate the elemental compositions and valence states of $NiCoP/NiCo_2S_4$. As shown in Fig. S4a, there is an extra P signal in the $NiCoP/NiCo_2S_4$ sample compared with the original $NiCo_2S_4$ sample. In the Ni 2p region (Fig. 4b), the spin orbitals located at 875.4 and 857.4 eV indicate the presence of Ni^{3+}, while the other two peaks centered at 871.1 and 853.8 eV prove the existence of Ni^{2+} [36,37]. In the case of the Co 2p spectrum (Fig. 4c), two strong peaks located at the binding energy of 798.5 and 782.6 eV confirm the presence of Co^{2+}, and the other two peaks at 794.0 and 779.1 eV prove the existence of Co^{3+} [38,39]. Therefore, the chemical composition of the as-prepared materials contain the cations of Ni^{2+}, Ni^{3+}, Co^{2+} and Co^{3+}. As for the S 2p spectrum (Fig. 4d), apart from the shake-up satellite peak at 169.3 eV, two peaks are located at 163.0 eV for S $2p_{1/2}$ and 161.8 eV for S $2p_{3/2}$, corresponding to the metal-sulfur (M–S) bonds in the samples [40,41]. In the P 2p region (Fig. 4e), the dominant peak located at 134.3 eV indicates that P exists mainly in the form of phosphate ions. And two peaks at 130.6 and 129.4 eV correspond to P $2p_{1/2}$ and P $2p_{3/2}$ spin orbitals [42,43], corresponding to metal phosphides. On the other hand, there is no signal in the P 2p region for pure $NiCo_2S_4$ sample. These results suggest that the heterostructured $NiCoP/NiCo_2S_4$ electrodes have been successfully prepared through the phosphate treatment with the NaH_2PO_2 as the phosphorus source.

The electrochemical performances of the as-prepared samples were evaluated on the three-electrode system with 1 mol L^{-1} KOH as the electrolyte. Fig. 5a shows the comparison cyclic voltammetry (CV) curves of the $NiCo_2O_4$, $NiCo_2S_4$, NiCoP and $NiCoP/NiCo_2S_4$ electrodes at the same scan rate of 10 mV s^{-1}. The current density and integral area of $NiCoP/NiCo_2S_4$ are much higher than that of the $NiCo_2O_4$, $NiCo_2S_4$, and NiCoP

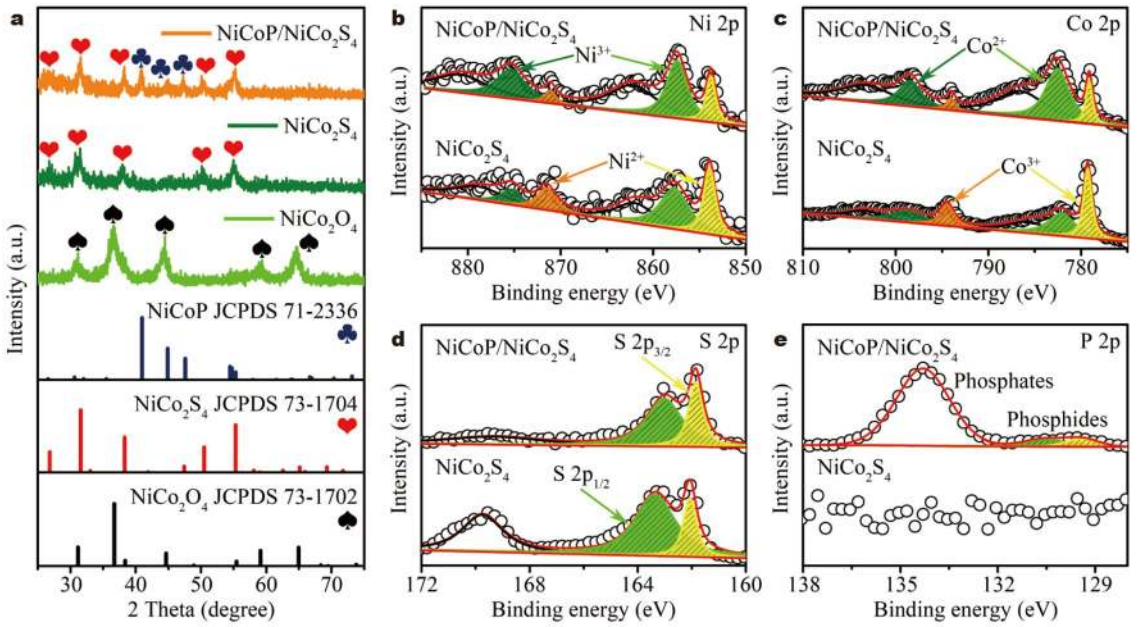

Figure 4 (a) XRD patterns of $NiCo_2O_4$, $NiCo_2S_4$ and NiCoP/$NiCo_2S_4$. (b) Ni 2p, (c) Co 2p, (d) S 2p and (e) P 2p core-level XPS spectra of $NiCo_2S_4$ and NiCoP/$NiCo_2S_4$.

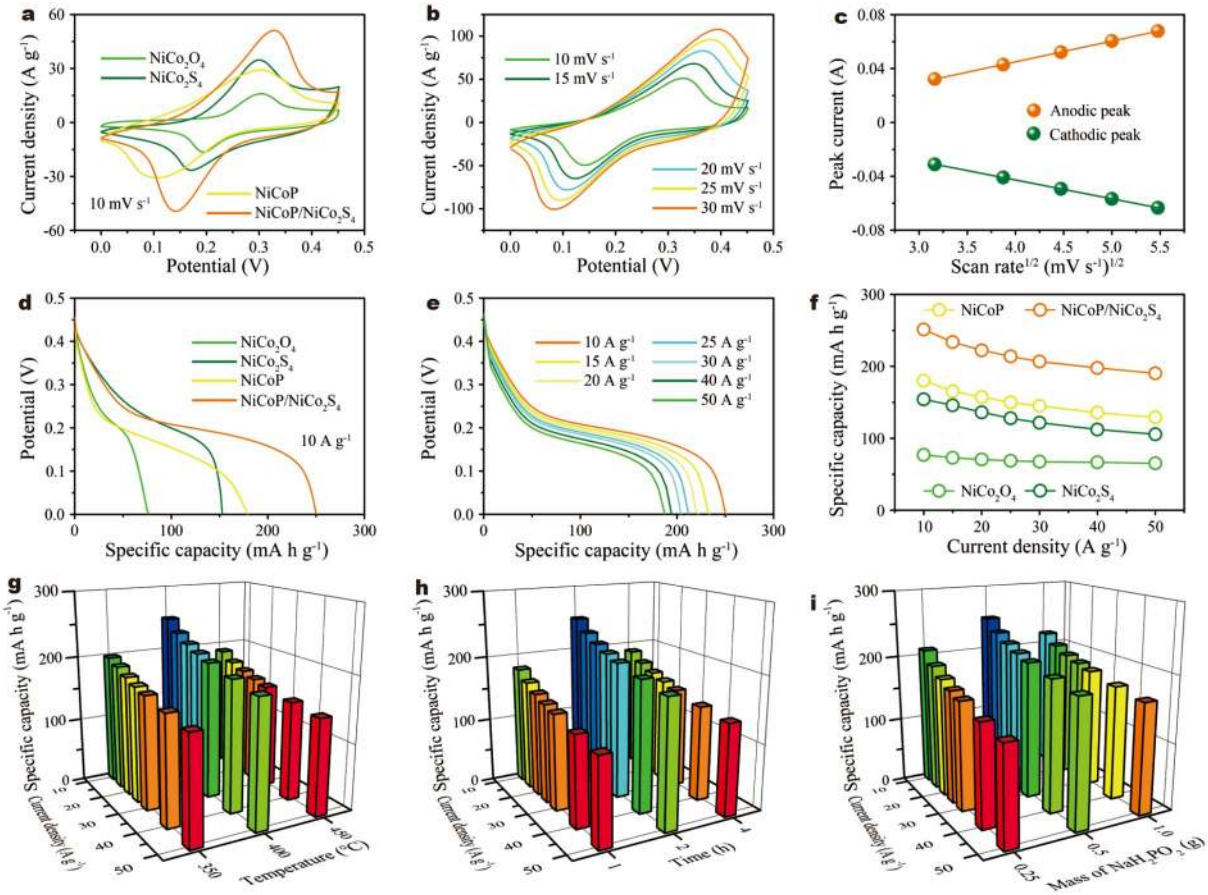

Figure 5 Comparison of (a) CV and (d) discharge curves of the $NiCo_2O_4$, $NiCo_2S_4$, NiCoP and NiCoP/$NiCo_2S_4$ electrodes. (b) CV and (e) discharge curves of the NiCoP/$NiCo_2S_4$ electrode. (c) Variation in the redox peak currents with the square root of the scan rates of the NiCoP/$NiCo_2S_4$ electrode. (f) Specific capacities *versus* current densities of the $NiCo_2O_4$, $NiCo_2S_4$, NiCoP and NiCoP/$NiCo_2S_4$ electrodes. Specific capacities of the NiCoP/$NiCo_2S_4$ electrodes as a function of (g) phosphating temperature, (h) reaction time and (i) mass of NaH_2PO_2.

electrodes, suggesting the enhanced specific capacity and faster redox reaction kinetics. As the scan rate increases from 10 to 30 mV s^{-1}, the CV curves of NiCoP/$NiCo_2S_4$ electrode remain symmetric redox peaks (Fig. 5b), indicating the great reversibility of redox reactions. As shown in Fig. 5c, there is a near linear relationship between peak currents and the square root of scan rates, demonstrating that the redox reactions for the NiCoP/$NiCo_2S_4$ electrode are diffusion-controlled [3,36]. The improved specific capacity can also be achieved by analyzing the discharge curves, as depicted in Fig. 5d, where the discharge plateau of the NiCoP/$NiCo_2S_4$ electrode is much longer than others at the same current density of 10 A g^{-1}. Additionally, in contrast to the $NiCo_2O_4$, $NiCo_2S_4$, and NiCoP electrodes, the discharge curves of the heterostructured NiCoP/$NiCo_2S_4$ remain steady discharge plateau as the current densities increase from 10 to 50 A g^{-1}, indicating the good rate performance (Fig. 5e and Fig. S5). The highest specific capacity obtained for the NiCoP/$NiCo_2S_4$ electrode is 251.1 mA h g^{-1} at a high current density of 10 A g^{-1} (Fig. 5f), which is higher than that of $NiCo_2O_4$ (76.9 mA h g^{-1}), $NiCo_2S_4$ (154.2 mA h g^{-1}) and NiCoP (180.0 mA h g^{-1}). Importantly, the NiCoP/$NiCo_2S_4$ electrode exhibits exceptional capacitive retention at a high current density. Even after increasing the current density to 50 A g^{-1}, the NiCoP/$NiCo_2S_4$ electrode shows a capacity of 190.3 mA h g^{-1}, which is about 76% retention of that at 10 A g^{-1}. The specific capacity of NiCoP/$NiCo_2S_4$ is close or even superior to many similar materials, such as Co_3S_4 (234.0 mA h g^{-1} at 8 A g^{-1}) [8], R-Co_3O_4 (212.6 mA h g^{-1} at 2 mA cm^{-2}) [18], Ni_3S_2@PANI (247.6 mA h g^{-1} at 11.4 A g^{-1}) [44], and $NiCo_2O_4$ (183.1 mA h g^{-1} at 1.6 A g^{-1}) [45]. Fig. 5g–i, Figs S6 and S7 show the electrochemical performances of the NiCoP/$NiCo_2S_4$ electrode under different phosphating conditions. It is clear that the optimal condition for the NiCoP/$NiCo_2S_4$ electrode is 400°C for 2 h with 0.5 g of NaH_2PO_2, which presents the highest specific capacity.

The outstanding specific capacity and high rate capability of the heterostructured NiCoP/$NiCo_2S_4$ electrode render it a great potential as the cathode in aqueous Zn-ion battery. An aqueous Zn-ion battery was assembled by using the NiCoP/$NiCo_2S_4$ electrode as the cathode and Zn plate as the anode with the mixed solution of 1 mol L^{-1} KOH and 0.01 mol L^{-1} $Zn(CH_3COO)_2$ as the electrolyte. The NiCoP/$NiCo_2S_4$ reacts with OH^- on the cathode, while reversible $Zn(OH)^{2-}/Zn^0$ stripping/plating occurs on the anode (Fig. 6a). Fig. 6b displays the CV curves of the NiCoP/$NiCo_2S_4$//Zn battery at various scan rates. Well-defined symmetric redox peaks can still be observed even at a high scan rate of 60 mV s^{-1}, revealing the highly reversible redox reaction. As shown in the charge-discharge curves of Fig. 6c, the discharge plateau of the NiCoP/$NiCo_2S_4$//Zn battery is approximately at 1.7 V. Additionally, the NiCoP/$NiCo_2S_4$//Zn battery shows better performances than the $NiCo_2S_4$//Zn battery (Fig. S8). Particularly, the NiCoP/$NiCo_2S_4$//Zn battery exhibits much higher specific capacity than the $NiCo_2S_4$//Zn battery, which is clearly demonstrated by comparing the CV and discharge curves (Fig. S9). Notably, the NiCoP/$NiCo_2S_4$//Zn battery yields an incredibly high specific capacity of 265.1 mA h g^{-1} at a high current density of 5 A g^{-1} (Fig. 6d), which is substantially higher than that of the $NiCo_2S_4$//Zn battery (144.3 mA h g^{-1}) and most reported Zn-ion batteries, such as $Ni(OH)_2$/CNFs//Zn (184 mA h g^{-1} at 5 mA cm^{-2}) [46], Co_3O_4//Zn (162 mA h g^{-1} at 1 A g^{-1}) [47], Ni_3S_2//Zn (148 mA h g^{-1} at 0.2 A g^{-1}) [48], NiO//ZnO (203 mA h g^{-1} at 0.5 mA cm^{-2}) [14], $NiCo_2O_4$//Zn (183.1 mA h g^{-1} at 1.6 A g^{-1}) [45], Zn//R-Co_3O_4 (240.8 mA h g^{-1} at 2 mA cm^{-2}) [18]. The NiCoP/$NiCo_2S_4$//Zn battery possesses a specific capacity of 139.7 mA h g^{-1} with ~53% capacity retention at 10 A g^{-1}, indicating its excellent rate capability. The high rate capability of the NiCoP/$NiCo_2S_4$//Zn battery was further demonstrated in Fig. 6e, where the current density increased from 5 to 10 A g^{-1} and returned to 5 A g^{-1}. The NiCoP/$NiCo_2S_4$//Zn battery delivers an average capacity of 264.9, 242.1, 206.2, 175.8, 155.2, and 139.7 mA h g^{-1} at 5, 6, 7, 8, 9, 10 A g^{-1}, respectively. When the current density is reduced back to 5 A g^{-1} after 50 cycles, the average capacity of 274.4 mA h g^{-1} is recovered, revealing excellent rate performance. Fig. 6f shows the long-term cycling performance of the NiCoP/$NiCo_2S_4$//Zn bat-

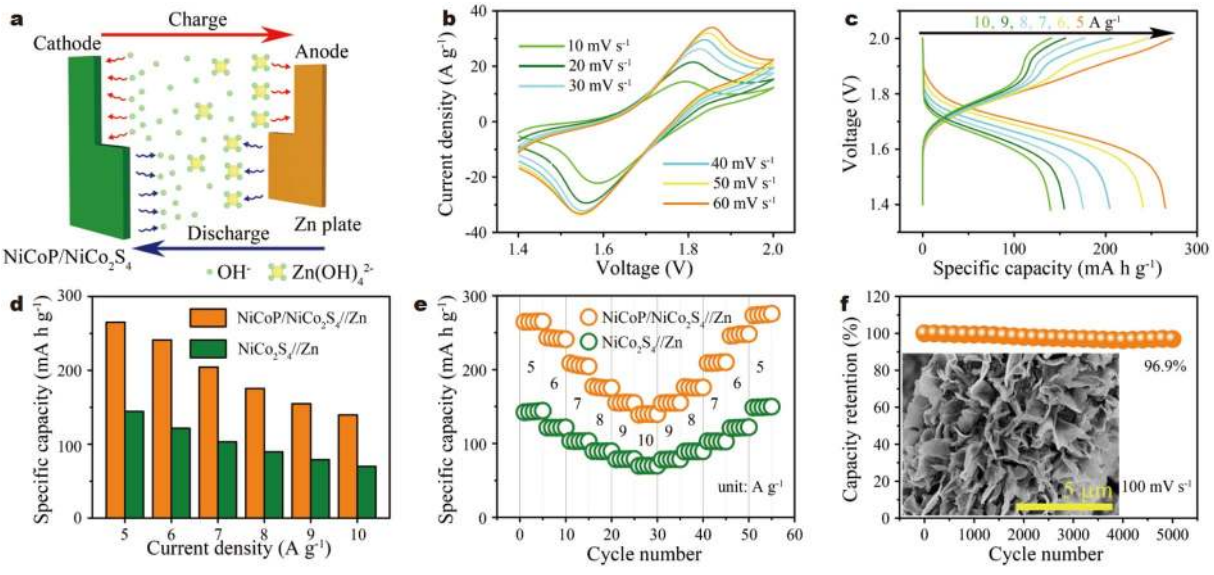

Figure 6 (a) Schematic diagram of the reaction mechanism of the NiCoP/$NiCo_2S_4$//Zn battery. (b) CV and (c) charge-discharge curves of the NiCoP/$NiCo_2S_4$//Zn battery. (d) Specific capacities *versus* current densities and (e) rate performances of the $NiCo_2S_4$//Zn and NiCoP/$NiCo_2S_4$//Zn batteries. (f) Cycling test of the NiCoP/$NiCo_2S_4$//Zn battery and the SEM image of the NiCoP/$NiCo_2S_4$ cathode after 5000 cycles (inset).

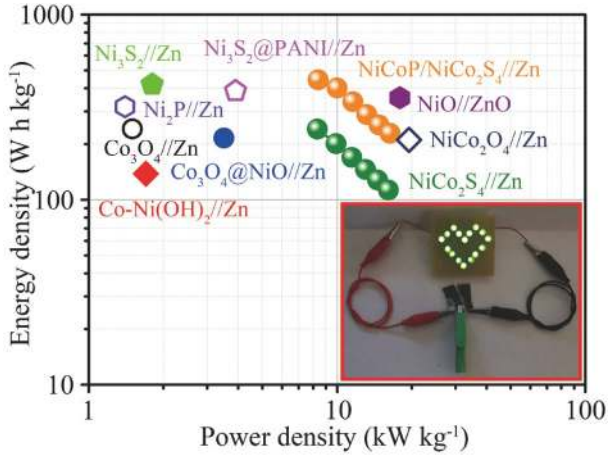

Figure 7 Ragone plots of the $NiCo_2S_4$//Zn battery and NiCoP/$NiCo_2S_4$//Zn battery compared with other similar studies. The inset is the digital photo of heart-shaped LEDs powered by two as-fabricated NiCoP/$NiCo_2S_4$//Zn batteries in series.

tery collected at a high scan rate of 100 mV s^{-1}. The NiCoP/$NiCo_2S_4$//Zn battery maintains 96.9% of the initial capacity after 5000 cycles. The NiCoP/$NiCo_2S_4$ nanosheet arrays are well-reserved (inset in Fig. 6f), further demonstrating the excellent cycling performance.

Energy density and power density are two important parameters to estimate the practicability of energy storage devices. Fig. 7 shows the Ragone plots of the as-assembled $NiCo_2S_4$//Zn battery and NiCoP/$NiCo_2S_4$//Zn battery. It can be observed that the NiCoP/$NiCo_2S_4$//Zn battery delivers a maximum energy density of 444.7 W h kg^{-1} at the power density of 8.4 kW kg^{-1}. When the power density is increased to 16.3 kW kg^{-1}, the energy density still remains 228.2 W h kg^{-1}. While the $NiCo_2S_4$//Zn battery only delivers a maximum energy density of 240.5 W h kg^{-1} at the power density of 8.3 kW kg^{-1}. The energy density of the obtained NiCoP/$NiCo_2S_4$//Zn battery is close to or even higher than those of some aqueous Zn-ion batteries reported previously, such as NiO//ZnO (355.7 W h kg^{-1} at 17.9 kW kg^{-1}) [14], Ni_2P//Zn (318.0 W h kg^{-1} at 1.4 kW kg^{-1}) [49], Ni_3S_2//Zn (419.6 W h kg^{-1} at 1.8 kW kg^{-1}) [48], Ni_3S_2@PANI//Zn (386.7 W h kg^{-1} at 3.9 kW kg^{-1}) [44], Co_3O_4//Zn (241.0 W h kg^{-1} at 1.5 kW kg^{-1}) [47], Co_3O_4@NiO//Zn (215.5 W h kg^{-1} at 3.5 kW kg^{-1}) [50], $NiCo_2O_4$//Zn (210.7 W h kg^{-1} at 19.5 kW kg^{-1}) [45], and Co-Ni$(OH)_2$//Zn (138.0 W h kg^{-1} at 1.7 kW kg^{-1}) [51]. The inset of Fig. 7 shows that two as-fabricated batteries connected in series can effectively power heart-shaped light-emitting diodes (LEDs) indicators, demonstrating the great promise for potential practical utilization.

CONCLUSION

In summary, we report the synthesis of heterostructured NiCoP/$NiCo_2S_4$ nanosheet arrays on carbon cloth through treating $NiCo_2S_4$ nanosheet arrays in the presence of P source, and demonstrate its excellent property as the electrode material in aqueous Zn-ion batteries. The high electrochemical activity between NiCoP and $NiCo_2S_4$ enables fast electron transport and rapid ion diffusion. As a result, the NiCoP/$NiCo_2S_4$ electrode shows a large specific capacity of 251.1 mA h g^{-1} at a high current density of 10 A g^{-1} and satisfactory rate capability (retaining about 76% even at 50 A g^{-1}). Furthermore, the assembled NiCoP/$NiCo_2S_4$//Zn battery delivers a high specific capacity of 265.1 mA h g^{-1} at 5 A g^{-1}, excellent cycling stability with 96.9% retention after 5000 cycles, as well as a competitive energy density of 444.7 W h kg^{-1} at the power density of 8.4 kW kg^{-1}. The successful construction of aqueous Zn-ion batteries by interfacial engineering of electrode materials sheds light on the exploration of high-performance energy storage devices in the future.

Received 29 April 2021; accepted 10 June 2021; published online 12 August 2021

1 Chen Y, Zhang W, Zhou D, *et al.* Co-Fe mixed metal phosphide nanocubes with highly interconnected-pore architecture as an efficient polysulfide mediator for lithium-sulfur batteries. ACS Nano, 2019, 13: 4731–4741
2 Fang G, Zhou J, Pan A, *et al.* Recent advances in aqueous zinc-ion batteries. ACS Energy Lett, 2018, 3: 2480–2501
3 Shen Y, Li Z, Cui Z, *et al.* Boosting the interface reaction activity and kinetics of cobalt molybdate by phosphating treatment for aqueous zinc-ion batteries with high energy density and long cycle life. J Mater Chem A, 2020, 8: 21044–21052
4 Liu J, Wang J, Ku Z, *et al.* Aqueous rechargeable alkaline $Co_xNi_{2-x}S_2$/TiO_2 battery. ACS Nano, 2016, 10: 1007–1016
5 Tang B, Shan L, Liang S, *et al.* Issues and opportunities facing aqueous zinc-ion batteries. Energy Environ Sci, 2019, 12: 3288–3304
6 Zhang K, Ye X, Shen Y, *et al.* Interface engineering of Co_3O_4 nanowire arrays with ultrafine NiO nanowires for high-performance rechargeable alkaline batteries. Dalton Trans, 2020, 49: 8582–8590
7 Huang M, Li M, Niu C, *et al.* Recent advances in rational electrode designs for high-performance alkaline rechargeable batteries. Adv Funct Mater, 2019, 29: 1807847
8 Zhang SW, Yin BS, Luo YZ, *et al.* Fabrication and theoretical investigation of cobaltosic sulfide nanosheets for flexible aqueous Zn/Co batteries. Nano Energy, 2020, 68: 104314
9 Liu J, Chen M, Zhang L, *et al.* A flexible alkaline rechargeable Ni/Fe battery based on graphene foam/carbon nanotubes hybrid film. Nano Lett, 2014, 14: 7180–7187
10 Jiao Y, Hong W, Li P, *et al.* Metal-organic framework derived Ni/NiO micro-particles with subtle lattice distortions for high-performance electrocatalyst and supercapacitor. Appl Catal B-Environ, 2019, 244: 732–739
11 Kim H, Jeong G, Kim YU, *et al.* Metallic anodes for next generation secondary batteries. Chem Soc Rev, 2013, 42: 9011–9034
12 Liu F, Chen Z, Fang G, *et al.* V_2O_5 nanospheres with mixed vanadium valences as high electrochemically active aqueous zinc-ion battery cathode. Nano-Micro Lett, 2019, 11: 25
13 Hu P, Wang T, Zhao J, *et al.* Ultrafast alkaline Ni/Zn battery based on Ni-foam-supported Ni_3S_2 nanosheets. ACS Appl Mater Interfaces, 2015, 7: 26396–26399
14 Liu J, Guan C, Zhou C, *et al.* A flexible quasi-solid-state nickel-zinc battery with high energy and power densities based on 3D electrode design. Adv Mater, 2016, 28: 8732–8739
15 Zeng Y, Meng Y, Lai Z, *et al.* An ultrastable and high-performance flexible fiber-shaped Ni-Zn battery based on a Ni-NiO heterostructured nanosheet cathode. Adv Mater, 2017, 29: 1702698
16 Tang Y, Li X, Lv H, *et al.* Stabilized Co^{3+}/Co^{4+} redox pair in *in situ* produced $CoSe_{2-x}$-derived cobalt oxides for alkaline Zn batteries with 10 000-cycle lifespan and 1.9-V voltage plateau. Adv Energy Mater, 2020, 10: 2000892
17 Gong M, Li Y, Zhang H, *et al.* Ultrafast high-capacity NiZn battery with nialco-layered double hydroxide. Energy Environ Sci, 2014, 7: 2025–2032
18 Lu Y, Wang J, Zeng S, *et al.* An ultrathin defect-rich Co_3O_4 nanosheet cathode for high-energy and durable aqueous zinc ion batteries. J Mater Chem A, 2019, 7: 21678–21683

19 Caldeira V, Rouget R, Fourgeot F, *et al.* Controlling the shape change and dendritic growth in Zn negative electrodes for application in Zn/Ni batteries. J Power Sources, 2017, 350: 109–116
20 Shen Y, Zhang K, Yang F, *et al.* Oxygen vacancies-rich cobalt-doped $NiMoO_4$ nanosheets for high energy density and stable aqueous Ni-Zn battery. Sci China Mater, 2020, 63: 1205–1215
21 Xiao J, Wan L, Yang S, *et al.* Design hierarchical electrodes with highly conductive $NiCo_2S_4$ nanotube arrays grown on carbon fiber paper for high-performance pseudocapacitors. Nano Lett, 2014, 14: 831–838
22 Shen L, Yu L, Wu HB, *et al.* Formation of nickel cobalt sulfide ball-in-ball hollow spheres with enhanced electrochemical pseudocapacitive properties. Nat Commun, 2015, 6: 6694
23 Guan BY, Yu L, Wang X, *et al.* Formation of onion-like $NiCo_2S_4$ particles *via* sequential ion-exchange for hybrid supercapacitors. Adv Mater, 2017, 29: 1605051
24 Zeng W, Zhang G, Wu X, *et al.* Construction of hierarchical CoS nanowire@$NiCo_2S_4$ nanosheet arrays *via* one-step ion exchange for high-performance supercapacitors. J Mater Chem A, 2015, 3: 24033–24040
25 Anwer H, Lee H, Kim HR, *et al.* Selective transport and separation of charge-carriers by an electron transport layer in $NiCo_2S_4$/CdO@CC for excellent water splitting. Appl Catal B-Environ, 2020, 265: 118564
26 Chen X, Chen D, Guo X, *et al.* Facile growth of caterpillar-like $NiCo_2S_4$ nanocrystal arrays on nickle foam for high-performance supercapacitors. ACS Appl Mater Interfaces, 2017, 9: 18774–18781
27 Shen Y, Zhang K, Chen B, *et al.* Enhancing the electrochemical performance of nickel cobalt sulfides hollow nanospheres by structural modulation for asymmetric supercapacitors. J Colloid Interface Sci, 2019, 557: 135–143
28 Han C, Zhang T, Li J, *et al.* Enabling flexible solid-state Zn batteries *via* tailoring sulfur deficiency in bimetallic sulfide nanotube arrays. Nano Energy, 2020, 77: 105165
29 Huang J, Xiong Y, Peng Z, *et al.* A general electrodeposition strategy for fabricating ultrathin nickel cobalt phosphate nanosheets with ultrahigh capacity and rate performance. ACS Nano, 2020, 14: 14201–14211
30 Liang H, Gandi AN, Anjum DH, *et al.* Plasma-assisted synthesis of NiCoP for efficient overall water splitting. Nano Lett, 2016, 16: 7718–7725
31 Nguyen TT, Balamurugan J, Kim NH, *et al.* Hierarchical 3D Zn-Ni-P nanosheet arrays as an advanced electrode for high-performance all-solid-state asymmetric supercapacitors. J Mater Chem A, 2018, 6: 8669–8681
32 Tian J, Liu Q, Asiri AM, *et al.* Self-supported nanoporous cobalt phosphide nanowire arrays: An efficient 3D hydrogen-evolving cathode over the wide range of pH 0–14. J Am Chem Soc, 2014, 136: 7587–7590
33 Song W, Wu J, Wang G, *et al.* Rich-mixed-valence $Ni_xCo_{3-x}P_y$ porous nanowires interwelded junction-free 3D network architectures for ultrahigh areal energy density supercapacitors. Adv Funct Mater, 2018, 28: 1804620
34 Zhang N, Li Y, Xu J, *et al.* High-performance flexible solid-state asymmetric supercapacitors based on bimetallic transition metal phosphide nanocrystals. ACS Nano, 2019, 13: 10612–10621
35 Li Y, Tan X, Tan H, *et al.* Phosphine vapor-assisted construction of heterostructured Ni_2P/$NiTe_2$ catalysts for efficient hydrogen evolution. Energy Environ Sci, 2020, 13: 1799–1807
36 Zeng Y, Lai Z, Han Y, *et al.* Oxygen-vacancy and surface modulation of ultrathin nickel cobaltite nanosheets as a high-energy cathode for advanced Zn-ion batteries. Adv Mater, 2018, 30: 1802396
37 Chu W, Shi Z, Hou Y, *et al.* Trifunctional of phosphorus-doped $NiCo_2O_4$ nanowire materials for asymmetric supercapacitor, oxygen evolution reaction, and hydrogen evolution reaction. ACS Appl Mater Interfaces, 2020, 12: 2763–2772
38 Tang S, Zhu B, Shi X, *et al.* General controlled sulfidation toward achieving novel nanosheet-built porous square-$FeCo_2S_4$-tube arrays for high-performance asymmetric all-solid-state pseudocapacitors. Adv Energy Mater, 2017, 7: 1601985
39 Wang Y, Chen Z, Lei T, *et al.* Hollow $NiCo_2S_4$ nanospheres hybridized with 3D hierarchical porous rGO/Fe_2O_3 composites toward high-performance energy storage device. Adv Energy Mater, 2018, 8: 1703453
40 Guan B, Li Y, Yin B, *et al.* Synthesis of hierarchical NiS microflowers for high performance asymmetric supercapacitor. Chem Eng J, 2017, 308: 1165–1173
41 Ye C, Zhang L, Guo C, *et al.* A 3D hybrid of chemically coupled nickel sulfide and hollow carbon spheres for high performance lithium-sulfur batteries. Adv Funct Mater, 2017, 27: 1702524
42 Chen HC, Jiang S, Xu B, *et al.* Sea-urchin-like nickel-cobalt phosphide/phosphate composites as advanced battery materials for hybrid supercapacitors. J Mater Chem A, 2019, 7: 6241–6249
43 Li S, Yang N, Liao L, *et al.* Doping β-$CoMoO_4$ nanoplates with phosphorus for efficient hydrogen evolution reaction in alkaline media. ACS Appl Mater Interfaces, 2018, 10: 37038–37045
44 Zhou L, Zhang X, Zheng D, *et al.* Ni_3S_2@PANI core-shell nanosheets as a durable and high-energy binder-free cathode for aqueous rechargeable nickel-zinc batteries. J Mater Chem A, 2019, 7: 10629–10635
45 Zhang H, Zhang X, Li H, *et al.* Flexible rechargeable Ni//Zn battery based on self-supported $NiCo_2O_4$ nanosheets with high power density and good cycling stability. Green Energy Environ, 2018, 3: 56–62
46 Jian Y, Wang D, Huang M, *et al.* Facile synthesis of $Ni(OH)_2$/carbon nanofiber composites for improving NiZn battery cycling life. ACS Sustain Chem Eng, 2017, 5: 6827–6834
47 Wang X, Wang F, Wang L, *et al.* An aqueous rechargeable Zn//Co_3O_4 battery with high energy density and good cycling behavior. Adv Mater, 2016, 28: 4904–4911
48 He Y, Zhang P, Huang H, *et al.* Engineering sulfur vacancies of Ni_3S_2 nanosheets as a binder-free cathode for an aqueous rechargeable Ni-Zn battery. ACS Appl Energy Mater, 2020, 3: 3863–3875
49 Wen J, Feng Z, Liu H, *et al. In-situ* synthesized Ni_2P nanosheet arrays as the cathode for novel alkaline Ni//Zn rechargeable battery. Appl Surf Sci, 2019, 485: 462–467
50 Lu Z, Wu X, Lei X, *et al.* Hierarchical nanoarray materials for advanced nickel-zinc batteries. Inorg Chem Front, 2015, 2: 184–187
51 Xu C, Liao J, Yang C, *et al.* An ultrafast, high capacity and superior longevity Ni/Zn battery constructed on nickel nanowire array film. Nano Energy, 2016, 30: 900–908

Acknowledgements This work was supported by the National Natural Science Foundation of China (51602049 and 51708504), and China Postdoctoral Science Foundation (2017M610217 and 2018T110322).

Author contributions Yang F and Shen Y performed the experiments and wrote the article; Cen Z and Wan J conducted the characterization and data analyses; Li S, He G, Hu J and Xu K proposed the experimental design and wrote the paper. All authors contributed to the general discussion.

Conflict of interest The authors declare that they have no conflict of interest.

Supplementary information Supporting data are available in the online version of the paper.

Fang Yang received her PhD degree from Donghua University in 2015. Currently, she works at the School of Mechanical and Automotive Engineering at Shanghai University of Engineering Science. Her research focuses on rational design and synthesis of nanocomposite materials for energy storage devices.

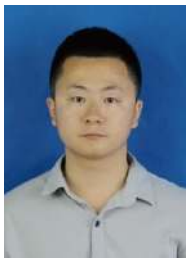

Shijie Li received his PhD degree in environmental engineering from Donghua University in 2014. He is currently an associate professor at the National Engineering Research Center for Marine Aquaculture, Zhejiang Ocean University. His research interests focus on the development of functional nanomaterials and their applications in electrochemical energy storage and conversion, and environmental remediation.

Kaibing Xu received his PhD degree from Donghua University in 2015. Currently, he works at the Research Center for Analysis and Measurement, Donghua University. His research focuses on rational design and synthesis of nanocomposite materials for applications in electrochemical energy storage and conversion such as supercapacitors, alkaline rechargeable batteries and lithium ion batteries.

原位构筑富异质结界面的双金属硫/磷化合物提升水系锌电池性能

杨方[1], 沈越年[2], 岑泽[1], 万杰[1], 李世杰[3*], 何冠杰[4], 胡俊青[2,5], 徐开兵[2*]

摘要 目前开发高倍率和稳定的水系锌离子电池电极材料仍然是一个挑战. 本研究提出了一种磷化辅助界面工程策略, 将$NiCo_2S_4$纳米片可控转化为NiCoP/$NiCo_2S_4$异质结构作为水系锌离子电池电极材料. 具有丰富界面的多组分异质结构不仅提高了电极材料的电导率, 而且增强了锌离子的扩散路径. 和预期结果一样, NiCoP/$NiCo_2S_4$电极材料在10 A g^{-1}的电流密度下其容量高达251.1 mA h g^{-1}, 且具有优异的倍率性能(电流密度高达50 A g^{-1}时, 其容量保持约为76%). 此外, 以NiCoP/$NiCo_2S_4$为正极组装的锌离子电池也展现了优异的比容量(在5 A g^{-1}的电流密度下高达265.1 mA h g^{-1}), 长循环稳定性(经过5000圈循环后比容量保持率为96.9%)和高能量密度(在8.4 kW kg^{-1}的功率密度下高达444.7 W h kg^{-1}). 因此, 本研究为构建具有丰富界面的异质结电极材料提供了一种简单的磷化辅助界面工程策略, 为未来开发高性能储能器件提供了理论基础.

